EcoSeis: A novel acquisition method for optimizing seismic resolution while minimizing environmental footprint

Mostafa Naghizadeh[1], Peter Vermeulen[1], Andrea Crook[1], Alyson Birce[1], Stephanie Ross[1], Aaron Stanton[2], Maximo Rodriguez[3], and Warren Cookson[4]

https://doi.org/10.1190/tle42010061.1

Abstract

All exploration and production projects, whether for oil-and-gas, mining, or clean-technology applications, begin with an accurate image of the subsurface. Many technologies have been developed to enable the acquisition of cost-effective seismic data, with high-density land seismic programs becoming commonplace. However, as the industry progresses and the long-term surface footprint associated with these programs becomes better understood, new methods are needed to reduce the environmental impact of seismic data acquisition while maintaining sufficient subsurface resolution for accurate resource development. New acquisition geometries are typically easier to create than test in the field due to the high cost of field acquisition and processing. However, by using existing data acquired in a grid, one can decimate the original data set into multiple geometries and process them. This provides an opportunity to fully test new geometries without the expense of field acquisition. In this paper, we present processing, interpretation, and inversion tests from an existing ultra-high-density oil-sands seismic data set decimated based on ecologically improved program designs. We then measure and compare the results to understand the impact of these geometries on subsurface resolution.

Introduction

Seismic exploration for oil and gas in Canada's boreal forests requires the clearing of trees along seismic lines to ensure safe access for equipment deployment (Crook et al., 2021). Depending on the distribution pattern of the seismic cutlines, the resulting footprint can result in cutting 10%–25% of the total program area. In general, these programs are typically acquired with an orthogonal geometry pattern that generates interconnected pathways and increases forest fragmentation. This negatively affects sensitive species. Seismic data acquisition activities can also result in soil compaction and a higher water table. This leads to elevated methane emissions (Strack et al., 2019) and increased greenhouse gas (GHG) emissions due to the removal of canopy, soil compaction, and associated emissions from equipment used for deployment of sources and receivers. Work is being done to reclaim old seismic lines, but this is expensive.

Some of the solutions that have been proposed to reduce the environmental impact of seismic programs include minimizing cutting by flying equipment in with a helicopter, utilizing alternative sampling theorems to reduce the amount of equipment needed, and miniaturizing seismic equipment (energy sources and/or receivers). Individually, these solutions can provide benefits such as reduced line widths and less overall cutting of the boreal forest, but habitat fragmentation due to interconnected seismic lines remains a problem. Additionally, in areas without forest cover, other environmental restrictions such as sensitive species and habitats may require a geometry with a lower land footprint. By moving to alternative-, irregular-, and linear-type geometries (Figure 1), the land footprint associated with seismic can be reduced. However, additional processing may be required to maintain sufficient subsurface resolution. A specific benefit of linear-type geometries is that they can be more cost effective to acquire in the field.

Technologies such as miniaturized sources and recording equipment as well as innovative cutting techniques are delivering encouraging results, but the next step toward ecologically intelligent seismic surveys has emerged in the world of seismic program design (Vermeulen et al., 2022). The focus of these new designs is to maximize subsurface resolution while minimizing the environmental impact. In forested regions, conventional seismic programs often require cutting trees to provide safe access for equipment deployment. Irregular or alternative geometries, such as those developed as part of the EcoSeis project, can reduce the total amount of line clearing within a seismic program by up to 55%. This reduction in land footprint also leads to a reduction in both GHG and methane emissions due to lower fuel consumption

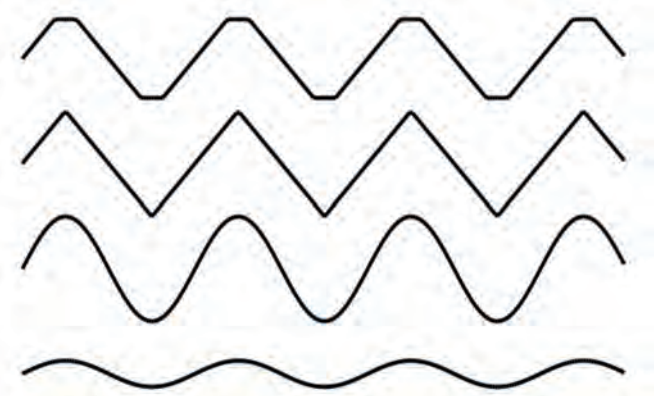

Figure 1. Four examples of linear geometries that can provide up to a 55% reduction in total footprint by eliminating the need to cut orthogonal seismic lines. Note that the distance between lines, amplitude, and frequency of the line pattern, as well as the distribution of sources along the lines, requires careful planning to ensure sufficient subsurface resolution.

[1]OptiSeis Solutions Ltd., Calgary, Alberta, Canada. E-mail: mostafa.naghizadeh@optiseis.com; peter.vermeulen@optiseis.com; andrea.crook@optiseis.com; alyson.birce@optiseis.com; stephanie.ross@optiseis.com.
[2]Key Seismic Solutions Ltd., Calgary, Alberta, Canada. E-mail: aaron.stanton@keyseismic.com.
[3]Qeye, Calgary, Alberta, Canada. E-mail: mr@qeye-labs.com.
[4]Cenovus Energy, Calgary, Alberta, Canada. E-mail: warren.cookson@cenovus.com.

and less ground compaction. This is beneficial for programs with and without seismic line cutting. Additionally, by reducing the overall environmental footprint of the seismic program, cost savings may be realized.

In this paper, we analyze the suitability of two alternative linear geometries to produce high-resolution seismic images compared to a conventional orthogonal geometry. Similar processing flows including 5D interpolation have been applied for the select geometries. Finally, the processed seismic volumes have been examined using a full seismic interpretation workflow to understand the shortcomings and advantages of each geometry.

Methodology and geometries

In this study, we used a very densely acquired real seismic data set (Geometry 0 [G0]) to examine the effectiveness of seismic data processing and interpolation algorithms on several decimated geometries (Figure 2a). G0 has a grid geometry with 20 m source, receiver, source-line, and receiver-line intervals. Although more than 20 different decimated geometries were tested during the project, for brevity, we will only discuss results from three of the geometries. The first geometry is orthogonal (G1) with 60 m line spacing and represents the typical orthogonal geometry for this area (Figure 2b). The second is a low trace density linear sinusoidal geometry (G2) with congruent lines spaced at 80 m (Figure 2c). The third geometry has linear zigzag lines (G3) with each zig and zag offset halfway from adjacent lines spaced at 60 m (Figure 1d). The G2 and G3 geometries have a weave pattern (Naghizadeh, 2015) that possesses suitable properties for sparse Fourier reconstruction algorithms. Figures 2e–2h show the fold distribution for the G0, G1, G2, and G3 geometries shown in Figures 2a–2d, respectively.

Figures 3a–3d show the polar azimuthal distribution of the midpoints in the offset range of 0–170 m for an 80 × 100 m area in the middle of surveys G0, G1, G2, and G3, respectively. Figures 3e–3h show the offset distributions of seismic traces corresponding to the plots in Figures 3a–3d, respectively. The G1 orthogonal and G3 zigzag geometries have equal trace densities. However, the G2 zigzag geometry has lower trace density compared to the other two geometries due to the larger line interval. The orthogonal geometry, G1, has a more uniform midpoint, offset, and azimuth distribution compared to the sinusoidal and zigzag geometries. On the other hand, these zigzag geometries require approximately 50% fewer cutlines compared to the orthogonal survey, leading to a significant reduction in environmental footprint.

Seismic data processing and interpolation

The amplitude variation with offset (AVO)-compliant processing of seismic data, including the static corrections and velocity estimation for the selected geometries (G0, G1, G2, and G3), was conducted from raw shots using only the available data for each decimated geometry. In this study, interpolation was applied using minimum weighted norm Fourier interpolation (Liu and Sacchi, 2004) in the 5D common-offset-vector (COV) domain. This algorithm uses sparsity promotion in the *f*-*k* domain to interpolate data along four spatial dimensions (inline, crossline,

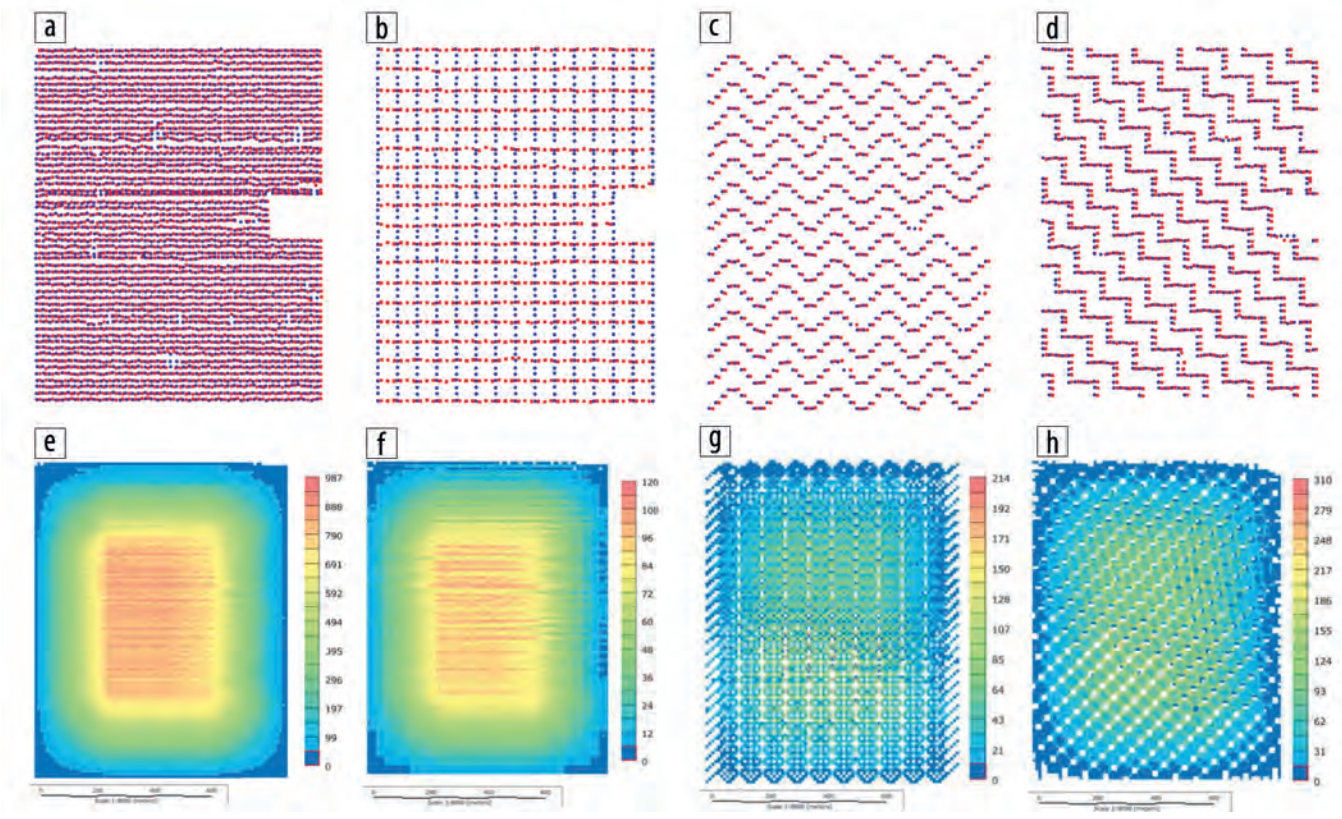

Figure 2. (a) Original densely acquired real seismic data geometry (G0). (b) Orthogonal geometry (G1) decimated from (a). (c) and (d) Zigzag geometries G2 and G3 decimated from (a), respectively. (e)–(h) Fold distribution for G0, G1, G2, and G3 geometries shown in (a)–(d), respectively.

inline offset, and crossline offset). The underlying assumption of this approach is that a multidimensional patch of data can be accurately represented by a small number of Fourier basis functions. The sparse Fourier domain recovery concept is closely related to the mathematical concept of compressive sensing/sampling (Candès, 2006; Candès and Wakin, 2008).

To implement interpolation in the COV domain, it is first necessary to define a suitable COV binning geometry for the data. For an orthogonal survey, the natural inline and crossline offset increments needed to achieve full subsurface coverage are twice the shot- and receiver-line spacings. For example, decimation G1, which has a shot- and receiver-line spacing of 60 m, has a natural inline and crossline offset increment of 120 m. However, applying 5D interpolation to the data using this COV geometry will not result in a significant uplift because the data are already fully sampled on the grid. Halving the inline and crossline offset increments to match the shot- and receiver-line increments reduces the number of live input traces to approximately 25%, which provides a reasonable interpolation target. Figure 4a displays the COV fold for geometry G1. While the fold of the near-offset COVs is high in a global sense, the sampling of the near offsets is highly variable across the survey as illustrated in Figures 4b–4e for geometries G0, G1, G2, and G3, respectively.

Figures 5a–5c depict the inline stack of input gathers going into 5D interpolation for G1, G2, and G3 geometries, respectively. Due to the linearity of the geometries, both G2 and G3 have gaps in the data at all target levels. However, the 5D interpolation was able to recover the missing traces and produce uniformly sampled gathers (Figures 5d and 5e). A qualitative inspection of the interpolated gathers shows that the main structure and texture of the seismic sections are well preserved after the interpolation. However, to fully understand the performance of interpolation for each geometry, it is necessary to examine the seismic volumes using full interpretation analysis.

Interpretation analysis

The high-density grid data set (G0) was acquired over a shallow oil-sands reservoir where steam-assisted gravity drainage well pairs were planned to produce bitumen from the sandy McMurray reservoir. Overlying the McMurray is the Clearwater marine shale unit that acts as the sealing cap rock as it contains steam and prevents a breach into shallower formations. The deposition of McMurray sands was strongly influenced by pre- and syndepositional karsting of the underlying Devonian carbonates from the dissolution of the Middle Devonian prairie evaporites. This left strong structural imprints on both formations of interest. High-density high-resolution seismic is typically acquired in this area to aid in creating detailed reservoir characterizations and to satisfy regulatory requirements, ensuring cap-rock integrity. Figure 6 shows a schematic representation of the stratigraphy and a well log in the study area. Top McMurray (MCMR) and Devonian (DVNN) formations are the main targets of this study

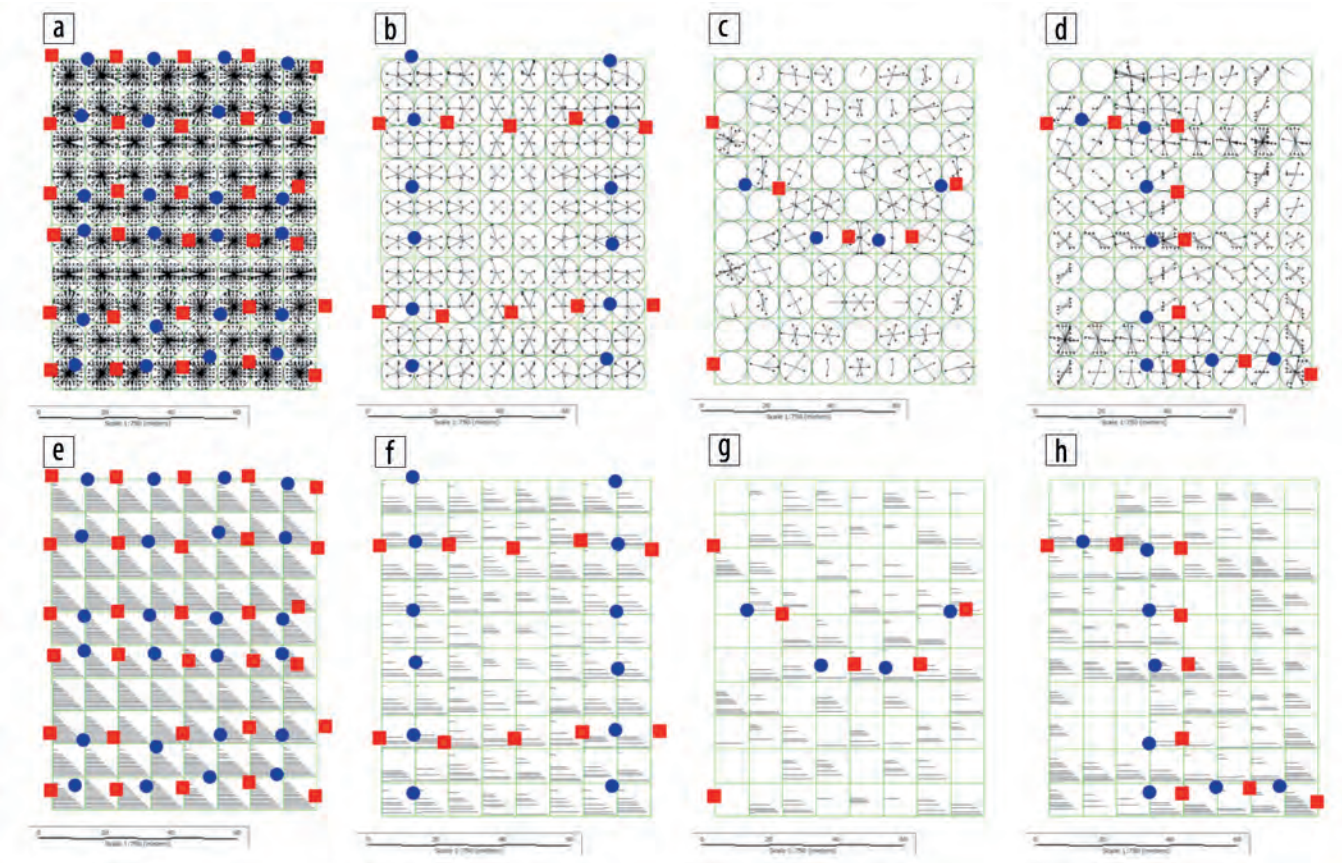

Figure 3. (a)–(d) Polar azimuthal distribution of the midpoints in the offset range of 0–168 m for an 80 × 100 m area in the middle of surveys G0, G1, G2, and G3, respectively. (e)–(h) Offset distributions of seismic traces corresponding to the plots in (a)–(d), respectively.

DOI:10.1190/tle42010061.1

and represent the top and base of the producing reservoir. We will compare the seismic attributes from these formation horizons for the decimated geometries.

Interpretation analysis began by seed picking the MCMR and DVNN horizons every 20th inline and 20th crossline, followed by 3D autopicking with matching parameters. The resulting time structures for the MCMR horizon are shown in Figures 7a–7d for G0, G1, G2, and G3 geometries, respectively. The G1 orthogonal geometry recovers the same regional details seen on the original G0 data set with minimal amounts of smear within finer structural features. The most sparsely sampled geometry, G2, struggles to autopick around the structural low in the northwest corner of the survey and smears most of the finer details throughout the rest of the survey. This indicates that there are limits to how large the line intervals can be spaced for a linear geometry. G3 had only minor challenges in autopicking around the structural low and did a much better job of recovering the smaller structural details seen in the undecimated survey.

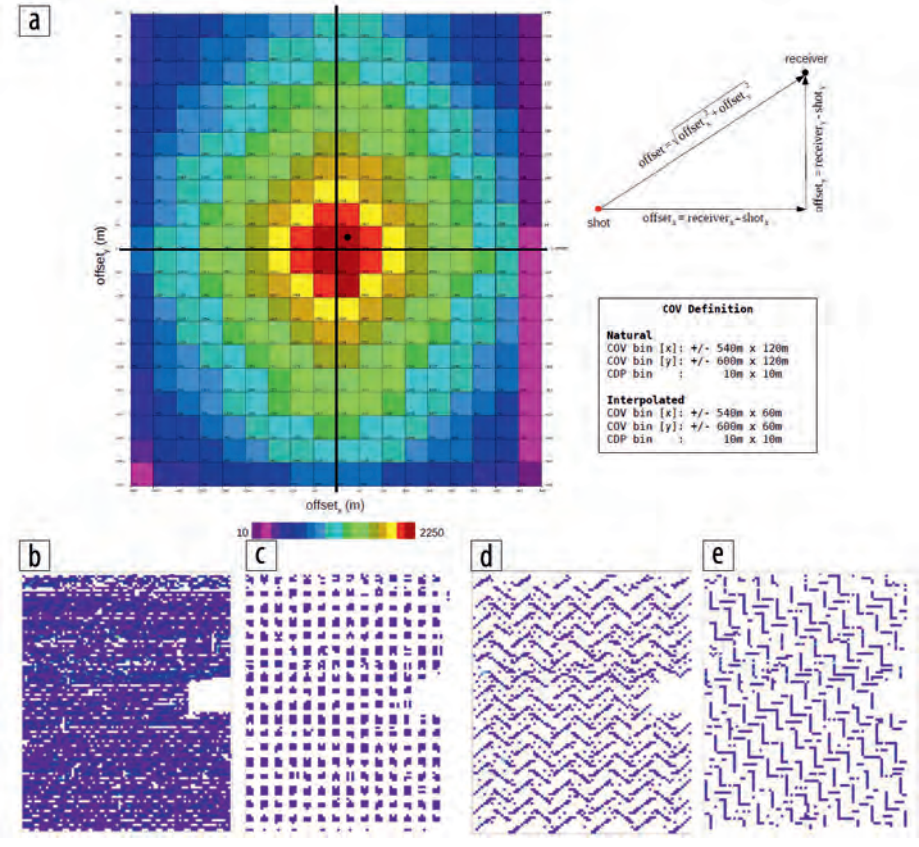

Figure 4. (a) Offset-vector tile grid used for 5D interpolation. (b)–(e) Midpoint distribution for a near-offset tile of offset-vector domain for G0, G1, G2, and G3, respectively.

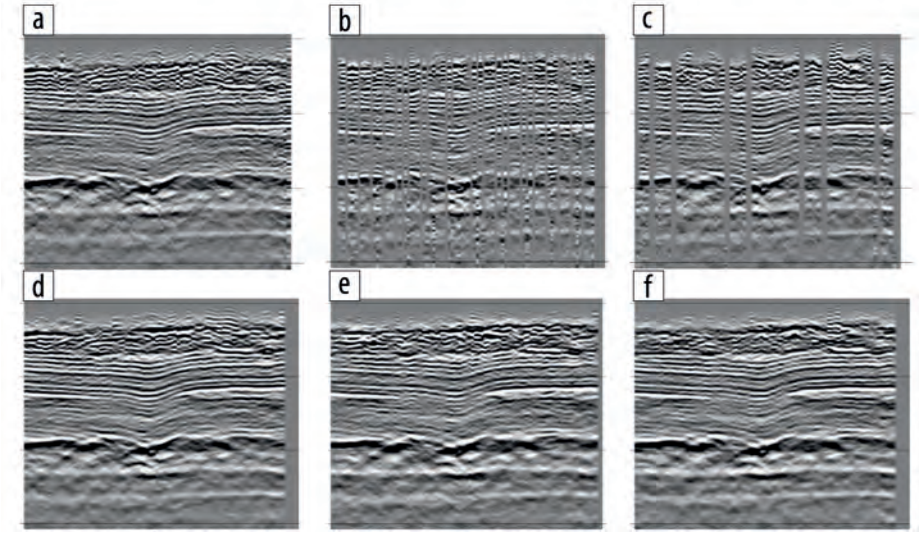

Figure 5. (a)–(c) The inline stack of input gathers for 5D interpolation for G1, G2, and G3 geometries, respectively. (d)–(f) Inline stack of output gathers from 5D interpolation for G1, G2, and G3 geometries, respectively.

The amplitude of the MCMR horizon reveals the impact that shallow acquisition footprints have on each geometry (Figures 7e–7h). G2 suffers the most due to the larger line interval (80 m) and the resulting sparser trace density, with a strong acquisition footprint that coincides with each trough and peak of the sinusoidal geometry. G1 and G3 have smaller acquisition footprints that impact MCMR resolution less than seen on G2.

Normalized root mean square (Nrms) was calculated within a zone 15 ms above and below the MCMR horizon to quantify and locate the differences between the geometries. Figures 7i–7k show the difference sections (Nrms changes) between G0 and the G1, G2, and G3 geometry amplitudes.

Phase stability and frequency content are important for understanding how the geometries compare. Figures 8a–8d show the instantaneous frequency slices and Figures 8e–8h show the instantaneous phase slices at MCMR horizon for G0, G1, G2, and G3 geometries, respectively. Lower trace density has the most detrimental effect on the frequency of the decimation, with G2 seeing a 5–10 Hz drop in frequency content at the MCMR level. G1 and G3 see smaller frequency drops but have a broader range of frequencies than G0 at the MCMR level.

The orthogonal geometry, G1, recovers similar phase to G0 with only a slight negative shift in values. G2, the sinusoidal geometry with lower trace density, has more significant phase changes with broader values and a shift in the negative direction. G3 also has

an increase in the phase range at the MCMR level but delivers a smaller change toward negative values, possibly due to its better near-offset distribution. When using alternative linear-type geometries such as G2 and G3, it is recommended that the design has proper trace density and near-offset distribution at the target horizon to ensure adequate subsurface resolution.

As we move to deeper targets such as the DVNN, the image differences start to disappear because trace density increases and

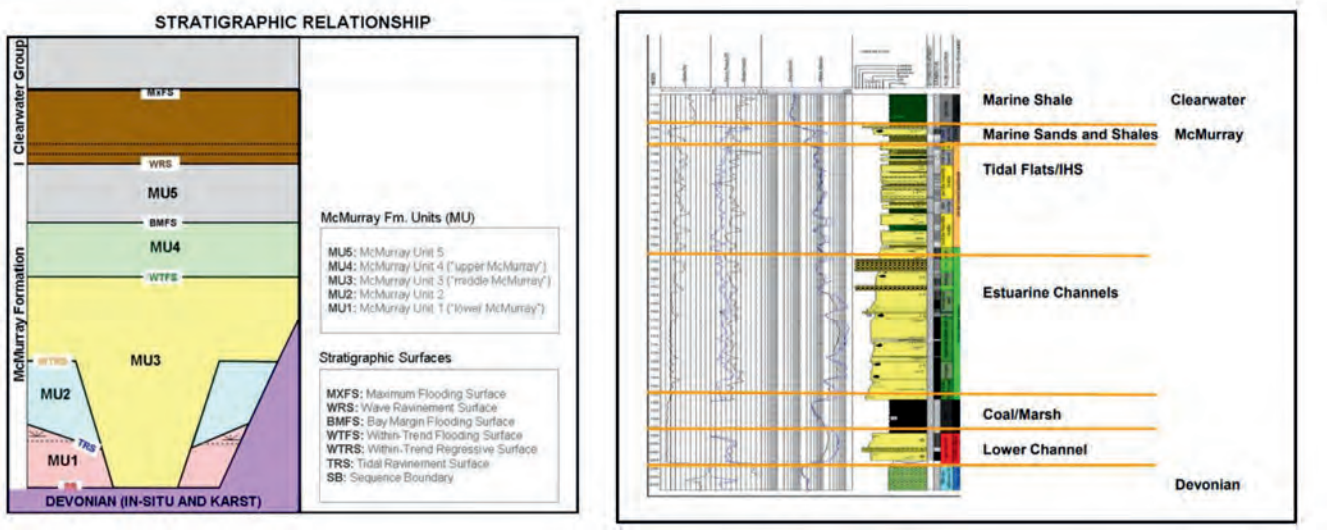

Figure 6. Schematic of the stratigraphic relationship and well log within the study area.

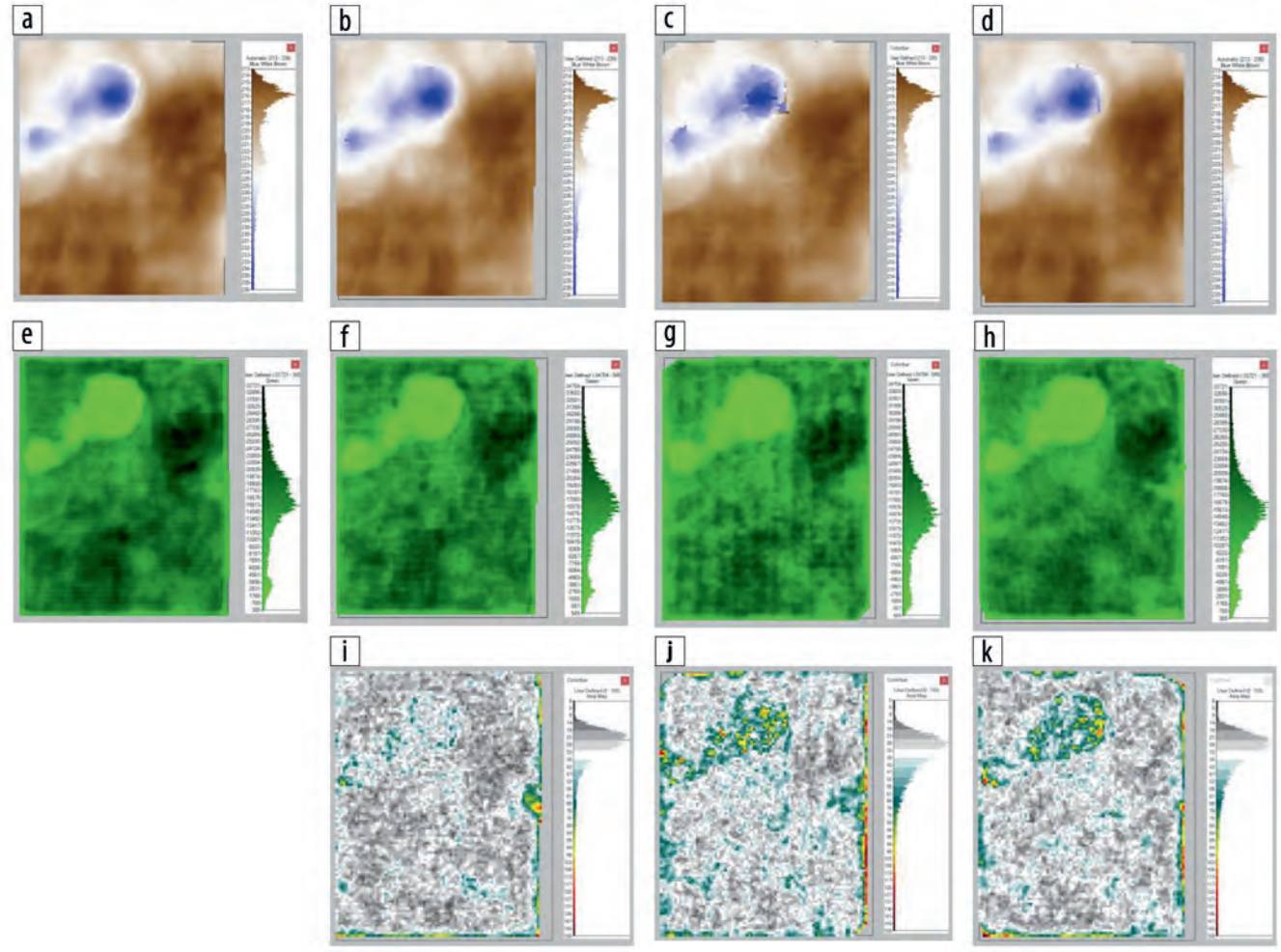

Figure 7. (a)–(d) Time structures at the MCMR horizon for G0, G1, G2, and G3 geometries, respectively. (e)–(h) The MCMR amplitude slides for G0, G1, G2, G3, respectively. (i)–(k) The difference sections generated by subtracting (f), (g), and (h) from (e), respectively.

the frequency of the data is slightly lower. The DVNN horizon is a highly structured surface with a collection of sinkhole structures underlying the reservoir of interest. The abrupt structural changes posed minor challenges for the autopicking, even on the original data set, G0, where we see small unpicked holes. Figures 9a–9d show the Devonian amplitude slides for G0, G1, G2, and G3 geometries, respectively. The autopicked DVNN horizon has slightly larger holes with unpicked traces, but G2 struggles less with this problem because there are fewer and smaller holes in the horizon. Imaging quality at DVNN is much more comparable between all decimations than in shallower horizons. G1 recovers most of the same details as G0 at the DVNN, and G2 and G3 are both comparable to G1 for large structural features, although they lose some resolution when imaging smaller sinkholes. Given the significant reduction in environmental footprint, these changes in resolution may be deemed acceptable.

Studying how the resolution changes between the data sets in the poststack domain only yields part of the answer. Most geophysical workflows now incorporate quantitative analysis to characterize reservoir properties, which provide a direct understanding of the geology. To complete our evaluation of the changes in resolution due to each geometry, G0, G1, G2, and G3 were taken through a quantitative analysis workflow, where acoustic impedance (Figures 10a–10d), V_P/V_S ratio (Figures 10e–10h), and density (Figures 10i–10l) attributes were calculated for each geometry using AVO simultaneous inversion. This prestack analysis delivered a deeper understanding of how the offsets and azimuths are populated within each decimation because missing offsets within specific angle ranges can hamper the inversion results and lead to the imprinting of acquisition footprints.

For the AVO inversion, all of the geometries were stacked in angle bands of 10° with an overlap of 2°, for a total of six angle stacks ranging from 0° to 58°. The prestack time migration (PSTM) velocities produced during the processing stage were used to transform the data from offset to angle domain. The same velocity field was used for angle stacking all of the geometries. This way, any changes in the quality of the angle stacks were the result of changes only in the offset distribution of each data set. The only preconditioning applied to the seismic data consisted of an angle-stack alignment process. This process maximized the local cross correlation between a reference angle

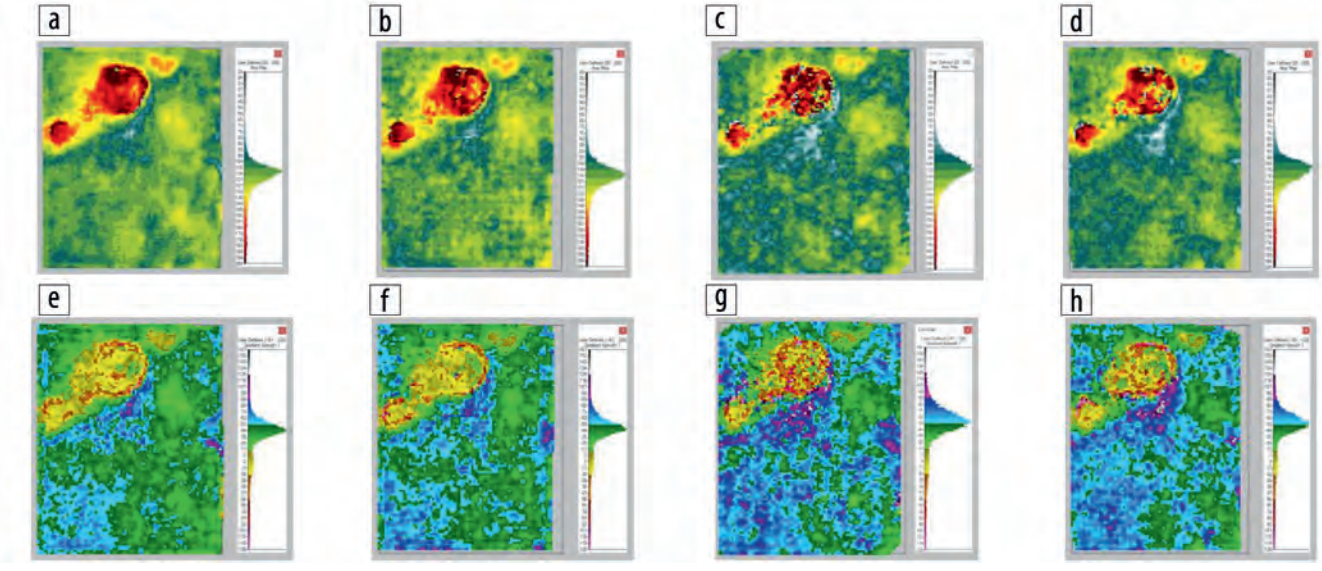

Figure 8. (a)–(d) The instantaneous frequency slices at MCMR for G0, G1, G2, and G3 geometries, respectively. (e)–(g) The instantaneous phase slices at MCMR for G0, G1, G2, and G3 geometries, respectively.

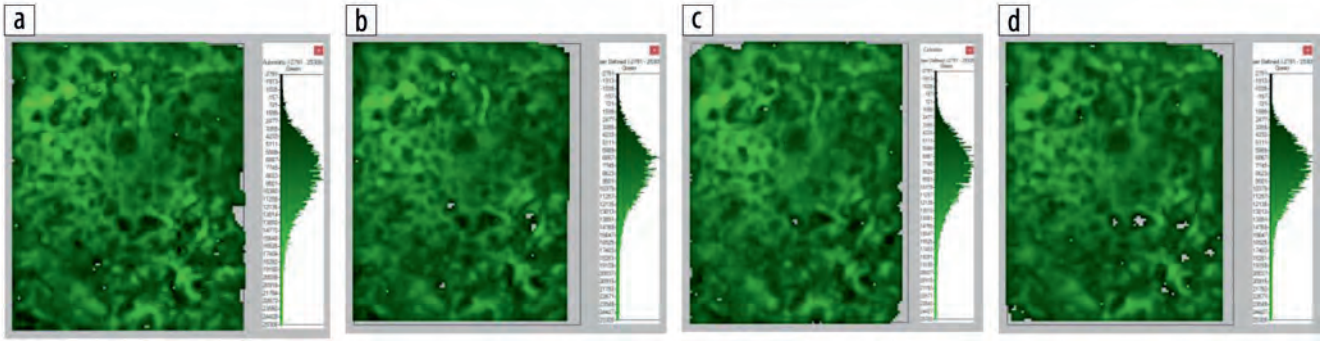

Figure 9. (a)–(d) The Devonian amplitude slides for G0, G1, G2, G3, respectively.

stack and all the available angle stacks using a smoothed time and space variant displacement field. The process attempts to remove any residual statics or residual moveout effects present in the data without altering the amplitude information.

Mutiwell angle-dependent wavelets were estimated using the data of the original geometry. A very simple low-frequency model was built by extrapolating the available log data over the entire volume using the seismic horizons as a guide. All of the inversions were conducted using the same set of wavelets and the same low-frequency model so that differences in the inversion results could be attributable to differences in the amplitudes of the angle stacks generated for each geometry. Geometries with a good near-offset distribution should have better acoustic impedance results because acoustic impedance relies on near-angle information to determine a solution. This can be seen with G3. It has a good distribution of near angles and produces acoustic impedance values closest to the original geometry. G1 and G2 have gaps within the near angles and as a result show more footprint in the acoustic impedance.

Elastic information in the form of the V_P/V_S ratio (closely linked to the amplitude gradients measured from the seismic volumes) shows even more variation between the geometries than the acoustic impedance plots. Here, we again see that G3 has a V_P/V_S ratio that is closest to the original data set, while G1 and G2 have stronger acquisition footprints.

The final inversion comparison is of the density results, which are particularly sensitive to far offsets and can degrade quickly above 40° depending on the quality of data. G1 and G2 underestimate the density and display a strong imprint of the acquisition geometry. The density solution for G3, however, compares much closer to the original geometry and does not have an acquisition footprint.

Overall, G3 geometry delivered better interpretation results in comparison to G1 and G2 geometries. The superior performance of G3 geometry is attributed to its abundant near-offset traces, adequate trace density, and the weave distribution pattern of sources and receivers. This led to suitable spatial sampling scenarios for sparse Fourier reconstruction or

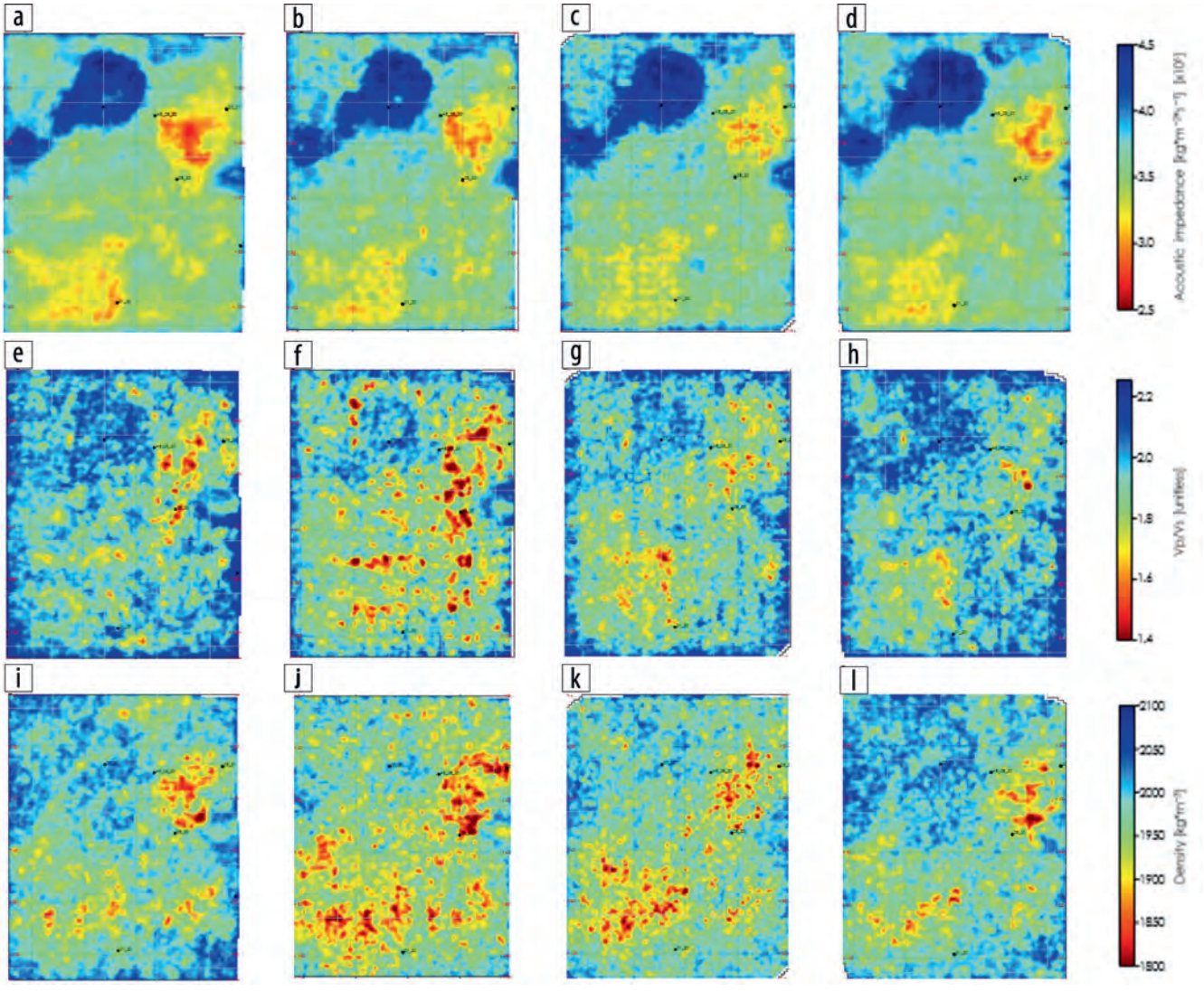

Figure 10. (a)–(d) The acoustic impedance attribute plots for G0, G1, G2, and G3 geometries, respectively. (e)–(h) The V_P/V_S attribute plots for G0, G1, G2, and G3 geometries, respectively. (i)–(l) The density attribute plots for G0, G1, G2, and G3 geometries, respectively.

compressive sensing algorithms (Naghizadeh and Sacchi, 2010; Naghizadeh, 2015).

Conclusions

Linear geometries, such as those illustrated in this case study, can provide a new way to acquire seismic data with a lower overall land footprint. Depending on the method of implementation, 55% or greater reductions in linear kilometers and total hectares cut can be achieved. In nonforested areas, the reduction in linear kilometers can increase operational efficiencies, resulting in cost savings and reduced emissions.

Here, we have shown that linear-type geometries can provide comparable results to conventional orthogonal geometries. However, converting a conventional orthogonal geometry to an alternative linear geometry requires careful consideration to ensure adequate imaging at all targets. The distance between lines, amplitude, and frequency of line variations (sinusoidal aspect) and the distribution of stations along the line play a part in determining the ultimate subsurface resolution. Although this paper analyzes land seismic geometries, these results are equally applicable in marine ocean-bottom-node surveys, which have similar geometry properties to land surveys. The next steps for this project will include a full-scale field test planned for late 2022 to evaluate the operational efficiency of implementing these types of linear geometries as well as further decimation tests exploring additional alternative linear and grid-type geometries. TLE

Acknowledgments

The authors would like to acknowledge Cenovus for use of the seismic data set for this research, Key Seismic Solutions Ltd. for processing the 3D data sets, OptiSeis for designing the tests and completing the interpretation, Qeye for the quantitative analysis, and other project collaborators for research-funding contributions.

Data and materials availability

Data associated with this research are confidential and cannot be released.

Corresponding author: mostafa.naghizadeh@optiseis.com

References

Candès, E. J., 2006, Compressive sampling: Proceedings of the International Congress of Mathematicians.

Candès, E. J., and M. B. Wakin, 2008, An introduction to compressive sampling: IEEE Signal Processing Magazine, **25**, no. 2, 21–30, https://doi.org/10.1109/MSP.2007.914731.

Crook, A., S. Bossaer, S. Contenti, C. Crook, K. Nwafor, and F. Sun, 2021, Case study: The use of miniaturized seismic sources for reduced environmental impact: 82nd Conference and Exhibition, EAGE, Extended Abstracts, https://doi.org/10.3997/2214-4609.202113189.

Liu, B., and M. D. Sacchi, 2004, Minimum weighted norm interpolation of seismic records: Geophysics, **69**, no. 6, 1560–1568, https://doi.org/10.1190/1.1836829.

Naghizadeh, M., 2015, Double-weave 3D seismic acquisition — Part 1: Sampling and sparse Fourier reconstruction: Geophysics, **80**, no. 6, WD143–WD162, https://doi.org/10.1190/geo2015-0161.1.

Naghizadeh, M., and M. D. Sacchi, 2010, On sampling functions and Fourier reconstruction methods: Geophysics, **75**, no. 6, WB137–WB151, https://doi.org/10.1190/1.3503577.

Strack, M., S. Hayne, J. Lovitt, G. J. McDermid, M. Rahman, S. Saraswati, and B. Xu, 2019, Petroleum exploration increases methane emissions from northern peatlands: Nature Communications, **10**, 2804, https://doi.org/10.1038/s41467-019-10762-4.

Vermeulen, P., A. Crook, M. Naghizadeh, and S. Ross, 2022, Turn your seismic program into a lean, green, resolution machine: Presented at GeoConvention.